Distinguishing intraplate from megathrust earthquakes using lacustrine turbidites

Maarten van Daele, Cristian Araya-Cornejo, Thomas Pille, Kris Vanneste, Jasper Moernaut, Sabine Schmidt, Philipp Kempf, Inka Meyer, Marco Cisternas

Submitted to Geology

Distinguishing intraplate from megathrust earthquakes using lacustrine turbidites

Maarten Van Daele[1], Cristian Araya-Cornejo[2,3], Thomas Pille[1], Jasper Moernaut[4], Kris Vanneste[5], Sabine Schmidt[6], Philipp Kempf[7,1], Inka Meyer[1] and Marco Cisternas[2]

[1]*Renard Centre of Marine Geology, Department of Geology, Ghent University, Gent, Belgium*

[2]*Escuela de Ciencias del Mar, Pontifícia Universidad Católica de Valparaíso, Valparaíso, Chile*

[3]*Observatorio de Gestión de Riesgo de Desastres, Universidad Bernardo O'Higgins, Santiago, Chile*

[4]*Institue of Geology, University of Innsbruck, Innsbruck, Austria*

[5]*Seismology & Gravimetry Section, Royal Observatory of Belgium, Brussels, Belgium*

[6]*UMR5805 EPOC, Université de Bordeaux, 33615 Pessac Cedex, France*

[7]*Geological Survey of Belgium, Royal Belgian Institute of Natural Sciences, Brussels, Belgium*

ABSTRACT

Subduction zone seismicity arises from megathrust, crustal and intraslab earthquakes, and understanding the recurrence patterns of each type is crucial for hazard assessments. Lake sediments can record earthquakes from all three seismogenic sources and thereby increase our understanding of potential temporal relations among them. Here we study the turbidite record of Lo Encañado, an Andean lake located in central Chile, just 40 km east of the country´s capital. We show that Lo Encañado turbidites can be attributed to (i) subaquatic slope failure by earthquake shaking (co-seismic), (ii) floods or human impact and (iii) post-seismic catchment

response. All historical earthquakes causing shaking intensities >VI have triggered co-seismic turbidites. While megathrust earthquakes triggered the thickest co-seismic turbidites, only the intraplate (intraslab and crustal) earthquakes triggered subaerial slope failures followed by post-seismic turbidites. We argue that this contrasting result is due to different spectra of seismic waves from these earthquake sources: higher-frequency accelerations from intraplate earthquakes are hardly attenuated in rocks around the lake, whereas lower-frequency accelerations from megathrust earthquakes are amplified in soft lake sediment. We test our findings by comparing acceleration response spectra of recent and historical intraslab and megathrust earthquakes along a longitudinal profile, and results suggest that Andean lakes are ideally located to distinguish earthquake sources.

INTRODUCTION

Seismic hazard in subduction zones arises from different types of earthquakes, including megathrust, crustal and intraslab earthquakes. Intraslab earthquakes are often normal-faulting events in the subducting slab at intermediate depth, such as the September 2017 Chiapas M8.2 and Puebla M7.1 Mexico earthquakes (~50 km deep; Segou and Parsons, 2018), which highlighted the significant hazard that these events pose. This is also the case in Chile, where the deadliest earthquake was the 1939 M8.3 Chillán intraslab event, instead of the giant 1960 M9.5 megathrust earthquake (Beck et al., 1998). Furthermore, it was proposed that the deadliest earthquake in colonial Chile, the 1647 Santiago earthquake, also had an intraslab source (Cisternas, 2012). These earthquakes barely cause surface deformation and often occur below the continent, they neither trigger significant tsunamis nor cause strong seismic shaking on the

45 continental slope. Coastal paleotsunami and deep marine paleoseismic records thus lack deposits
46 of these earthquakes.
47 Lakes are reliable quantitative paleoseismic recorders. In south-central Chilean lakes, the
48 distribution of turbidites (triggered by megathrust earthquakes) is mainly controlled by shaking
49 intensity (Moernaut et al., 2014; Van Daele et al., 2015). In New Zealand, a higher intensity
50 threshold for subaerial compared to subaquatic slope failure allowed to estimate rupture locations
51 along the Alpine Fault (Howarth et al., 2014). While such constant criteria are valid when
52 comparing earthquakes from the same fault (either megathrust, intraslab or crustal), they may not
53 be valid when comparing earthquakes sourced from different fault systems.
54 Here we present the turbidite record of Lo Encañado Lake (central Chilean Andes). We
55 examine whether megathrust, intraslab and crustal earthquakes can be distinguished based on the
56 turbidite record, which would open perspectives for seismogenic source identification.
57
58 **SETTING**
59 Central Chile has historically been struck by damaging megathrust, intraslab and crustal
60 earthquakes (Beck et al., 1998; Leyton et al., 2010). During the last century the study area
61 experienced three large megathrust earthquakes (1906 M_w 8.2, 1985 M_w 8.0 and 2010 M_w 8.8)
62 (Beck et al., 1998; Moreno et al., 2012), one intraslab event (1945 M_w 7.1) (Leyton et al., 2010)
63 and one crustal earthquake (1958 M_w 6.3) (Alvarado et al., 2009) (Fig. 1e).
64 We analyzed the sedimentary record of Lo Encañado, (33.7°S; 70.3°W; 2492 m a.s.l.), a
65 small lake (0.5 km²) located in the Central Chilean Andes, 40 km east of Santiago (Fig. 1a) (7
66 million inhabitants). It has a maximum depth of ~32 m, and a relatively large catchment (39 km²)
67 (Fig. 1b-d) that is entirely composed of Cenozoic continental volcanic rocks with low-grade

metamorphic mineral assemblages dominated by mafic phyllosilicates (mixed-layer chlorite/smectite) (Robinson et al., 2004). The southern part of the catchment is dominated by a canyon with a meandering stream, the northern part consists of steep rocky slopes with colluvium. About 90% of the catchment is drained by a single stream that builds a delta at the northern fringe of the lake. Negra Lake drained into Lo Encañado (Fig. 1b,c) until 1917, when an aqueduct bypass was constructed. Maximum river discharge of the downstream Maipo River occurs during austral spring and summer (i.e. Nov-Feb; DGA, Chilean Government).

METHODS

This section provides an overview of the methods used, more detailed information is available in the Data Repository (footnote 1).

Side-scan sonar data (Klein3000) provided an image of the bathymetry and sedimentary environment (channels, roughness). We collected sixteen 0.5-1.5 m long cores in order to understand the depositional processes that produced lacustrine turbidites. Cores were analyzed using a Geotek multi-sensor core logger (line scans, magnetic susceptibility logs, reflectance spectroscopy) and a Siemens Somatom Definition Flash (X-ray computed tomography). Master core ENC12-03 was additionally analyzed for granulometry of the clastic fraction (Malvern Mastersizer 3000) and loss on ignition. ENC12-04, a replica of the master core, was scanned with an itrax XRF core scanner.

The age model is a combination of (i) $^{210}Pb_{xs}$ dating (AD 1958.9 – 2010.2) supported by the southern hemisphere ^{137}Cs fallout peak in 1964 (Fig. DR1), and (ii) a floating varve chronology (AD 1905.7 – 1958.9) that is tied to the first widely detectable ^{137}Cs fallout around 1954. All dates are treated and plotted as decimal years AD.

Modified Mercalli Intensities (MMI) at the lake were estimated using published empirical attenuation relationships (see Data Repository).

In order to examine the general differences in spectral acceleration during megathrust and intraslab earthquakes in the study area, we compared acceleration response spectra (5% damping) from two recent earthquakes along a transect of seismic stations from the coast to the Andes (Fig. 1a). The two analyzed earthquakes, the 24 April 2017 M6.9 megathrust (Ruiz et al., 2017) and the 2 August 2017 M5.5 intraslab (Centro Sismológico Nacional: http://evtdb.csn.uchile.cl/) events, occurred at a similar latitude, just north of Lo Encañado, and caused very similar peak ground accelerations in the closest station (FAR1). We further modeled acceleration response spectra of these and other historical or hypothetical earthquakes using the empirical relation of Idini et al. (2017) for the Chilean subduction zone, which has different equations for megathrust and intraslab earthquakes.

Surface characteristics in the catchment were analyzed at a 10 m resolution using the 560 nm and 665 nm reflectance bands obtained by Sentinel 2. Data was analyzed using the ESA Sentinel Application Platform (SNAP).

SEDIMENTOLOGY AND TURBIDITE STRATIGRAPHY

The hemipelagic sediments of Lo Encañado are laminated. Those that accumulated in the first decades of the 20th century are dominated by siliciclastic material forming clastic varves (Zolitschka et al., 2015), with the coarse-grained lamina formed in spring and summer; when river discharge is highest (Fig. 2), and the fine-grained lamina during winter, when the lake freezes. The sediments become gradually more organic-rich between 1920 and 1960, resulting in increasingly diffuse laminae afterwards (Data Repository).

In the depocenter, turbidites are intercalated with the hemipelagic sediments. The turbidites do not have erosive bases, as evidenced by CT data and core-to-core correlation (Fig. 2 and DR2). The age-depth model allows correlation between all but one of the turbidites with a thickness ≥ 1 cm to historical events, such as earthquakes, floods and anthropogenic activities (see below). All historical ages are within a year of the central tendency of the modeled age distributions (Table DR2). Turbidites stand out as graded deposits, often with a homogeneous middle part. They are composed of more (coarse-grained) siliciclastic material and less aquatic algae such as diatoms than the hemipelagic sediments. Such composition is also reflected by higher magnetic susceptibility. The turbidites can be subdivided in three categories:

- Category 1 (C1) turbidites are directly covering slumps in cores located at the base of subaquatic slopes. They are characterized by (i) their brownish color, (ii) poor (basal) sorting, (iii) high basal D_{90}, and (iv) variable thickness distribution, resulting in a basin-focused geometry (Fig. 2, DR2 and DR3).

  These features (except for the color) are characteristic for lacustrine turbidites triggered by earthquakes (Beck, 2009). The genetic link with slumps on multiple slopes provides an additional argument (synchronicity criterion;) for a coseismic origin of the C1 turbidites. The age-depth model permits correlation of the five C1 turbidites in the record to five earthquakes, which are the only ones that caused MMIs >VI at the lake (i.e. AD 1906, 1945, 1958, 1985 and 2010; Fig. 2), similar to MMI thresholds determined by previous studies on Chilean (Moernaut et al., 2014; Van Daele et al., 2015) and small Alpine lakes (Wilhelm et al., 2016);
- Category 2a (C2a) turbidites also occur near the base of slopes, but are unrelated to slumps. They are distinguished by their (i) greyish color, (ii) low Fe/Ti, (iii) moderate

R_{560}/R_{665}, (iv) good sorting, (v) low D_{90} of the basal sediments, and (iv) relatively constant thickness throughout the basin (draping) (Fig. 2, DR2 and DR3).

The latter three characteristics are indicative of a flood trigger (Beck, 2009). The most prominent C2a turbidites correspond to peaks in maximum monthly discharge of the Maipo River farther downstream, caused by both high summer rainfall (1978, 1982?) and extreme autumn rain/snowmelt events (1982?, 1993) (Fig. 2). Others (e.g., 1917 aqueduct construction) are linked to anthropogenic activity (see also Data Repository);

- Category 2b (C2b) turbidites show the same textural and spatial characteristics as C2a turbidites, but have a more blueish color, higher Fe/Ti and R_{560}/R_{665}. They always occur within 0-2 cm above a C1 turbidite, suggesting a genetic link (Fig. 2, DR2 and DR3).

Despite their flood signature, C2b turbidites do not correlate to extreme discharge maxima. Their co-occurrence with co-seismic C1 turbidites can be explained by a catchment response in the form of post-seismic turbidites, as identified in New Zealand (Howarth et al., 2014) and other Chilean lakes (Van Daele et al., 2015). This hypothesis is supported by the striking similarity in – blue – color of areas in the catchment where active slope erosion exposed fresh (unweathered) rock, (Fig. 3). The bluish color is related to the high R_{560}/R_{665} reflectance ratio (Fig. 3), which can be explained by the presence of chlorites and absence of carotenoid pigments and iron oxides (see Data Repository for details). The higher Fe/Ti values of C2b turbidites likely result from limited iron leaching in the freshly exposed rocks compared to soils. We thus argue that the C2b turbidites are the result of post-seismic flooding of

sediment from co-seismic subaerial rock falls and slides. In this relatively dry climate we cannot exclude a few years delay, depending on the timing of the first occurrence of flood-like conditions (i.e. relatively high amount of rainfall in a few days) following the earthquake.

INTRASLAB VERSUS MEGATHRUST EARTHQUAKES

All earthquakes causing shaking intensities >VI at the lake triggered subaquatic slope failures and, hence, C1 turbidites. In contrast, we were not able to define a minimum intensity for triggering subaerial slope failures and consequently C2b turbidites.,The 1945 intraslab earthquake (~VI½) triggered onshore slope failures whereas the 1906 and 2010 megathrust earthquakes (~VI½-VII) did not (Fig. 2, Table DR3). Even though intensities >VI are indeed sufficient to trigger slope failures such as disrupted slides and rock falls in some regions (Keefer, 1984), this does not explain the respective absence or presence of post-seismic turbidites for the megathrust and intraplate earthquakes. The finding of Antinao and Gosse (2009) that crustal seismicity in the region is a more important rockslide trigger than megathrust earthquakes provides a clue, but they did not consider intraslab seismicity.

We therefore explore the possible influence of the spectral characteristics of earthquake ground motion (due to source, path and site effects) on the presence or absence of onshore slope failures. The stress drop for a given magnitude is much higher for crustal (Allmann and Shearer, 2009) and intraslab (Leyton et al., 2009) earthquakes than for megathrust earthquakes, resulting in a higher corner frequency, and thus a higher-frequency source spectrum (Ruiz and Saragoni, 2008). Moreover, due to the longer travel distance to the lake (>150 km vs <100 km; Table DR3), seismic waves originating at the megathrust will experience more attenuation of

183 particularly the high-frequency components (e.g., Anderson and Hough, 1984) than crustal and
184 intraslab-sourced waves.
185 This reasoning is supported by the response spectra from the 2017 megathrust and
186 intraslab earthquakes (Fig. DR5). Especially at the Andean station (FAR1; Fig. 1a) – where the
187 difference in travel distance between different earthquake types is largest – the response
188 spectrum of the intraslab earthquake peaks at higher frequencies (>5 Hz) than that of the
189 megathrust event (<5 Hz) (Fig. 4a, DR5). These spectra indicate that intraslab earthquakes have
190 a greater potential to trigger onshore rock failures than megathrust earthquakes in the study area.
191 On the other hand, soft lake sediments amplify low-frequency accelerations (Fig. 4b) (Seed et al.,
192 1976), and megathrust earthquakes are thus more likely to trigger subaquatic slope failures.
193 Modeled response spectra for hypothetical (Data Repository) and historical (Fig. 4c) intraslab
194 and megathrust earthquakes (1945, 1985 and 2010) further support this hypothesis; if a Chiapas-
195 like earthquake (M8.2, Mexico 2017) would occur at an epicentral distance of 200 km it would
196 still likely trigger both on- and offshore failures and thus be recorded as an intraplate earthquake.
197 The Lo Encañado turbidite record is the first to permit differentiation between
198 seismogenic sources based on their specific source signal. While at present we can distinguish
199 megathrust from intraplate earthquakes, additional records will be required to distinguish
200 intraslab from crustal earthquakes, as the former affect a larger area and should thus be
201 evidenced in other Andean lakes.
202
203 **ACKNOWLEDGMENTS**
204 MVD acknowledges the financial support from the Research Foundation – Flanders (FWO), the
205 IAS Postgraduate Grant Scheme and the GSA Limnogeology Division for the Kerry Kelts

206 award; CA, JM and MC from the Chilean FONDECYT project 1150321, MC from Millennium
207 Nucleus The Seismic Cycle Along Subduction Zones funded by the Millennium Scientific
208 Initiative (NC160025) and Moernaut by the Austrian Science Fund (FWF) (project P30285-
209 N34). We thank S. Barrientos and R. Urrutia for facilitating fieldwork, and W. Vandoorne, A.
210 Peña and P. Guzmán for help on the field. R. Achten is acknowledged for use of the CT scanner.
211

212 **REFERENCES CITED**

213 Allmann, B. P., and Shearer, P. M., 2009, Global variations of stress drop for moderate to large
214 earthquakes: Journal of Geophysical Research, v. 114, no. B1. doi:
215 10.1029/2008jb005821
216 Alvarado, P., Barrientos, S., Saez, M., Astroza, M., and Beck, S., 2009, Source study and
217 tectonic implications of the historic 1958 Las Melosas crustal earthquake, Chile,
218 compared to earthquake damage: Physics of the Earth and Planetary Interiors, v. 175, no.
219 1-2, p. 26-36
220 Anderson, J. G., and Hough, S. E., 1984, A model for the shape of the Fourier amplitude
221 spectrum of acceleration at high frequencies: Bulletin of the Seismological Society of
222 America, v. 74, no. 5, p. 1969-1993
223 Antinao, J. L., and Gosse, J., 2009, Large rockslides in the Southern Central Andes of Chile (32–
224 34.5°S): Tectonic control and significance for Quaternary landscape evolution:
225 Geomorphology, v. 104, no. 3-4, p. 117-133. doi: 10.1016/j.geomorph.2008.08.008
226 Beck, C., 2009, "Late Quaternary lacustrine paleo-seismic archives in north-western Alps:
227 Examples of earthquake-origin assessment of sedimentary disturbances": Earth-Science
228 Reviews, v. 96, no. 4, p. 327-344. doi: 10.1016/j.earscirev.2009.07.005

229 Beck, S., Barrientos, S., Kausel, E., and Reyes, M., 1998, Source characteristics of historic
230 earthquakes along the central Chile subduction zone: Journal of South American Earth
231 Sciences, v. 11, no. 2, p. 115-129
232 Howarth, J. D., Fitzsimons, S. J., Norris, R. J., and Jacobsen, G. E., 2014, Lake sediments record
233 high intensity shaking that provides insight into the location and rupture length of large
234 earthquakes on the Alpine Fault, New Zealand: Earth and Planetary Science Letters, v.
235 403, p. 340-351. doi: 10.1016/j.epsl.2014.07.008
236 Idini, B., Rojas, F., Ruiz, S., and Pastén, C., 2017, Ground motion prediction equations for the
237 Chilean subduction zone: Bulletin of Earthquake Engineering, v. 15, no. 5, p. 1853-1880.
238 doi: 10.1007/s10518-016-0050-1
239 Keefer, D. K., 1984, Landslides caused by earthquakes: Bulletin of the Geological Society of
240 America, v. 95, no. 4, p. 406-421
241 Leyton, F., Ruiz, J., Campos, J., and Kausel, E., 2009, Intraplate and interplate earthquakes in
242 Chilean subduction zone: A theoretical and observational comparison: Physics of the
243 Earth and Planetary Interiors, v. 175, no. 1-2, p. 37-46. doi: 10.1016/j.pepi.2008.03.017
244 Leyton, F., Ruiz, S., and Sepúlveda, S. A., 2010, Reevaluación del peligro sísmico probabilístico
245 en Chile central: Andean geology, v. 37, p. 455-472
246 Moernaut, J., Van Daele, M., Heirman, K., Fontijn, K., Strasser, M., Pino, M., Urrutia, R., and
247 De Batist, M., 2014, Lacustrine turbidites as a tool for quantitative earthquake
248 reconstruction: New evidence for a variable rupture mode in south central Chile: Journal
249 of Geophysical Research: Solid Earth, v. 119, p. 1607-1633. doi: 10.1002/2013JB010738
250 Moreno, M., et al., 2012, Toward understanding tectonic control on the Mw 8.8 2010 Maule
251 Chile earthquake: Earth and Planetary Science Letters, v. 321-322, no. 0, p. 152-165

252 Robinson, D., Bevins, R. E., Aguirre, L., and Vergara, M., 2004, A reappraisal of episodic burial
253 metamorphism in the Andes of central Chile: Contributions to Mineralogy and Petrology,
254 v. 146, no. 4, p. 513-528. doi: 10.1007/s00410-003-0516-4
255 Ruiz, S., et al., 2017, Nucleation Phase and Dynamic Inversion of the Mw 6.9 Valparaíso 2017
256 Earthquake in Central Chile: Geophysical Research Letters, v. 44, no. 20, p. 10,290-
257 210,297. doi: 10.1002/2017GL075675
258 Ruiz, S., and Saragoni, R. G., 2008, Two peaks response spectra (2PRS) for subduction
259 earthquakes considering soil and source effects, The 14th World conference on
260 Earthquake Engineering: Bejing, China, p. 8.
261 Seed, H. B., Ugas, C., and Lysmer, J., 1976, Site-dependent spectra for earthquake-resistant
262 design: Bulletin of the Seismological Society of America, v. 66, no. 1, p. 221-243
263 Segou, M., and Parsons, T., 2018, Testing earthquake links in Mexico from 1978 up to the 2017
264 M=8.1 Chiapas and M=7.1 Puebla shocks: Geophysical Research Letters, v. 45, p. n/a-
265 n/a. doi: 10.1002/2017GL076237
266 Van Daele, M., et al., 2015, A comparison of the sedimentary records of the 1960 and 2010 great
267 Chilean earthquakes in 17 lakes: Implications for quantitative lacustrine
268 palaeoseismology: Sedimentology, v. 62, no. 5, p. 1466-1496. doi: 10.1111/sed.12193
269 Wilhelm, B., et al., 2016, Quantified sensitivity of small lake sediments to record historic
270 earthquakes: Implications for paleoseismology: Journal of Geophysical Research: Earth
271 Surface, v. 120. doi: 10.1002/2015jf003644
272 Zolitschka, B., Francus, P., Ojala, A. E. K., and Schimmelmann, A., 2015, Varves in lake
273 sediments – a review: Quaternary Science Reviews, v. 117, p. 1-41. doi:
274 10.1016/j.quascirev.2015.03.019

Figures

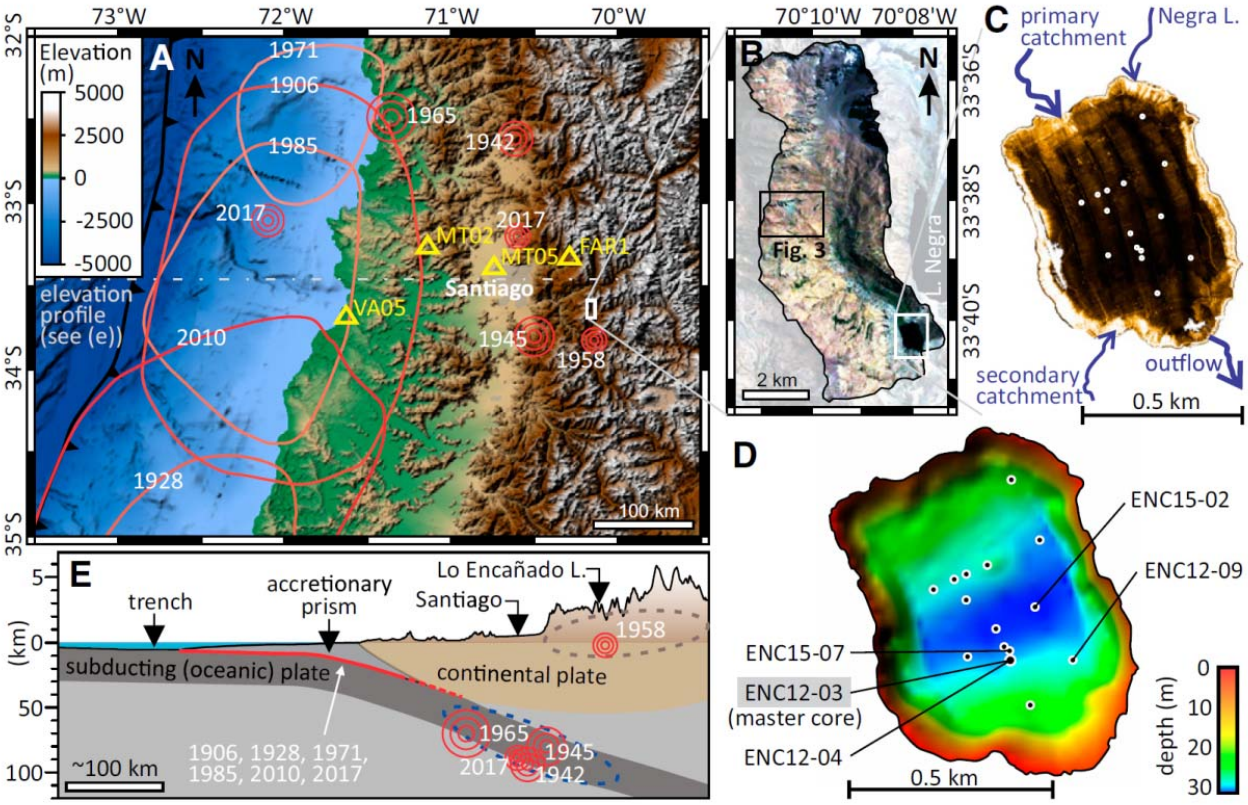

Figure 1: (a) map of central Chile showing epicenters (red circles) and rupture areas (reddish lines) of major historical intraplate and megathrust earthquakes, respectively, as well as epicenters of two 2017 earthquakes and seismic stations (yellow triangles); (b) histogram equalized satellite imagery (Google Earth) of the Lo Encañado Lake's catchment; (c) side-scan sonar mosaic (black = low reflectivity) of Lo Encañado showing core locations (white circles) and main river in- and outflows; (d) bathymetry showing core locations and names; (e) schematic profile at latitude of Santiago (see (a)) with indication of the three main seismogenic sources:

megathrust (red line), intraslab (blue dashed ellipse) and crustal (brown dashed ellipse); and their associated historical earthquakes.

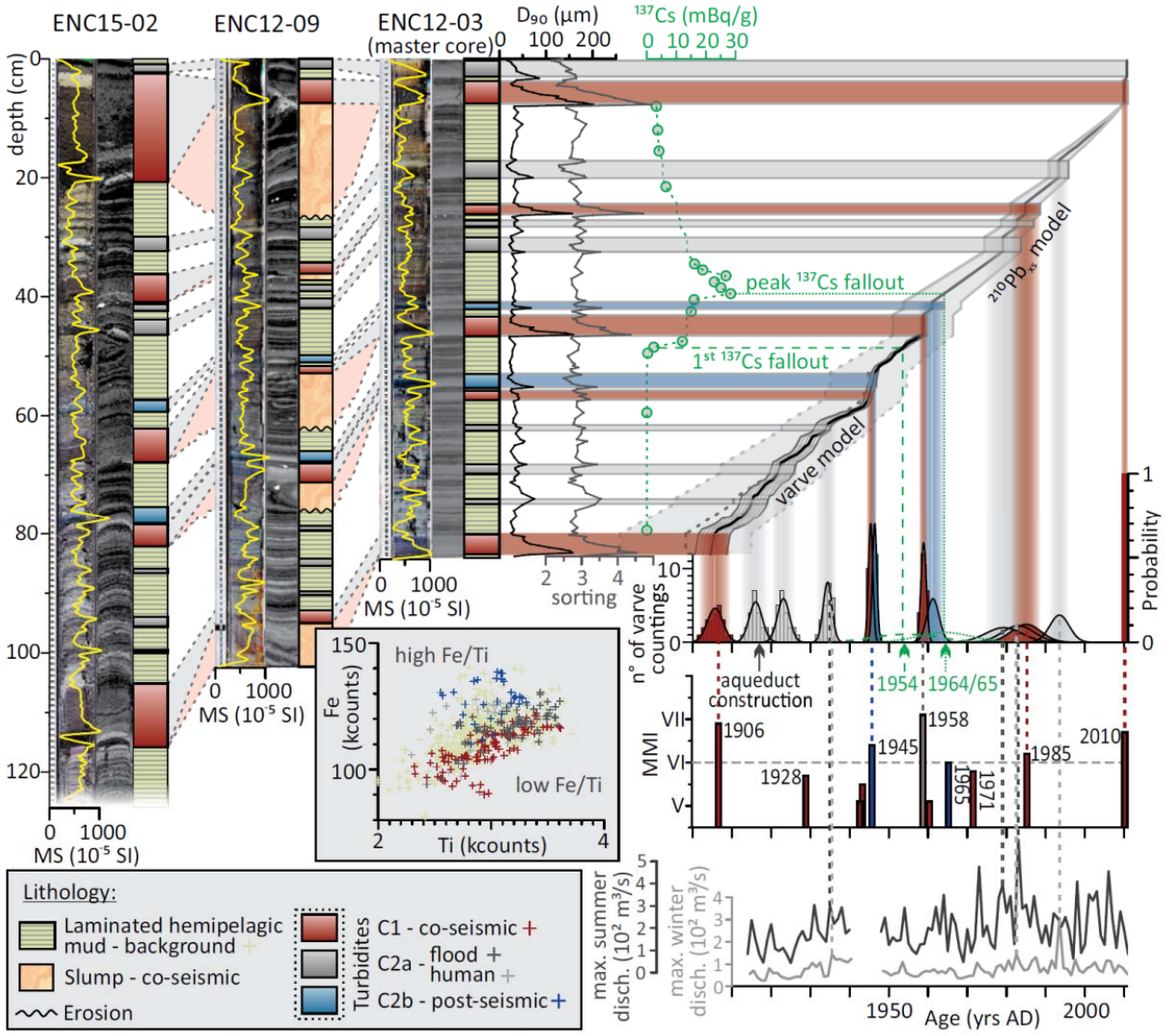

Figure 2: Left: cores ENC15-02, ENC12-09 and ENC12-03 with for each (from left to right): histogram equalized core image with magnetic susceptibility (MS, yellow line), CT scan view along core surface and lithotype. Right (top): for core ENC12-03: grain-size parameters D_{90} and sorting, ^{137}Cs activity, combined $^{210}Pb_{xs}$ and varve age model (uncertainties are 1 SD), and

(below) probability density functions for all turbidites based on the combined age model. Right (bottom): Modified Mercalli Intensity (MMI) for the historical earthquakes as calculated from empirical attenuation relationships (see Data Repository) and (below) maximum monthly summer and winter discharge in the Maipo River downstream of Lo Encañado Lake: station El Ingenio (1913-1940) and El Manzano (1947-2016). Middle: XRF Fe versus Ti counts of different lithologies in core ENC12-04.

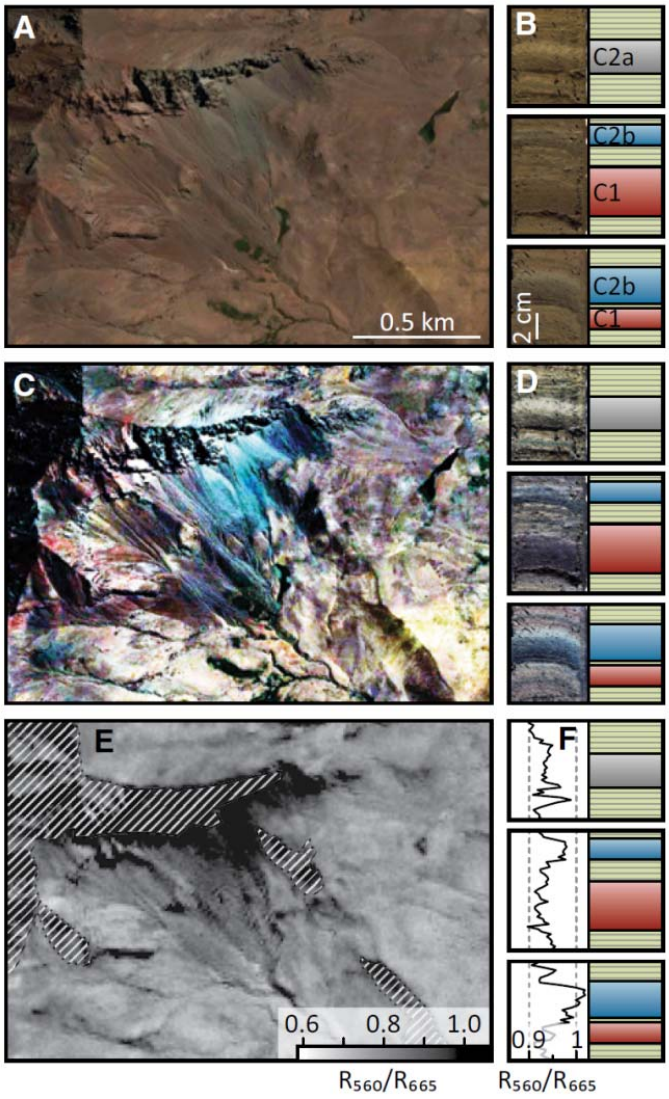

Figure 3: Color and spectral reflectance comparison to identify sediment source. Satellite imagery (Google Earth) (a, c) and reflectance (e; Copernicus Sentinel data 2018) of active slope processes in the Lo Encañado Lake catchment (location: Figure 1b). Core image (b, d) and reflectance (f) of three sections in ENC15-07 with lithotype (location: Figure DR4). Images (a) and (b) are in unprocessed colors, in (c) and (d) color differences are enhanced using histogram equalization. The spectral bandwidth of the reflectance data is similar in (e) and (f): ~35 nm for the 560 nm band (R_{560}) and ~30 nm for the 665 nm band (R_{665}).

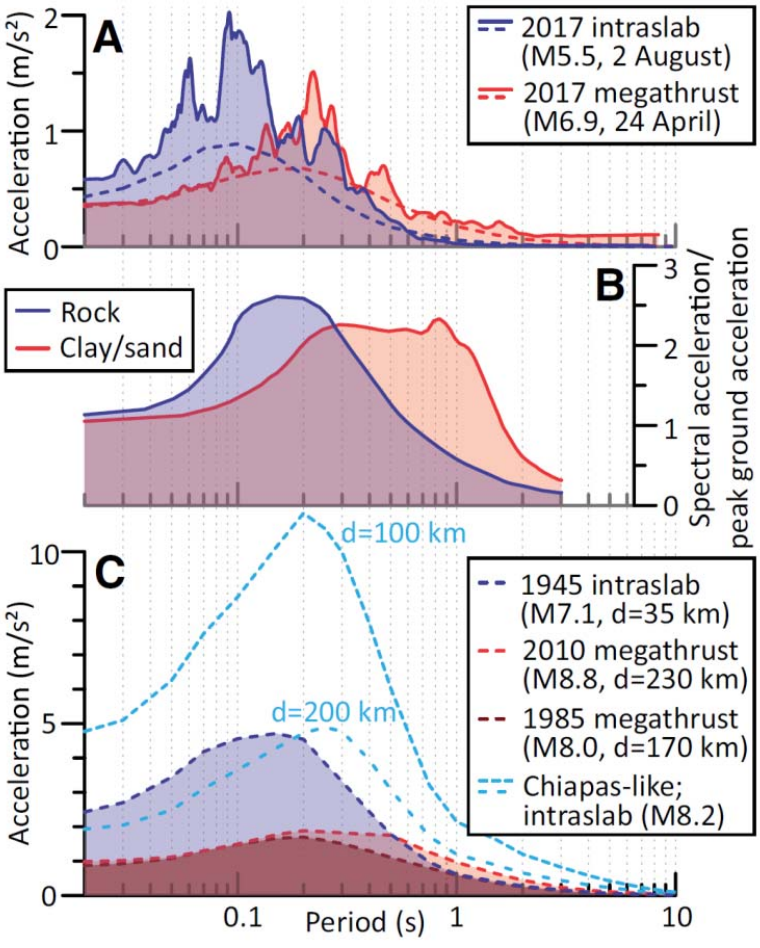

Figure 4: (a) Acceleration response spectra (5% damping) at the Andean seismic station FAR1 (location: Figure 1a) for the 2017 intraslab and megathrust earthquakes, both computed from accelerograms (solid lines) and modeled using the ground-motion prediction equation of Idini et al. (2017) (dashed lines); (b) average normalized acceleration response spectra (5% damping) for "rock" and "soft to medium stiff clays with associated strata of sands or gravels" in the western United States, after Seed et al. (1976); (c) modeled acceleration response spectra (5% damping) at Lo Encañado Lake for the 1945 intraslab and 2010 and 1985 megathrust earthquakes, as well as for a Chiapas-like intraslab earthquake (Sept. 2017, Mexico) at 100 and 200 km distance.

GSA Data Repository item 2019050 – DOI 10.1130/G45662.1

Distinguishing intraplate from megathrust earthquakes using lacustrine turbidites

M. Van Daele et al.

METHODS

Sedimentology

Cores were retrieved during three field seasons (2011, 2012 and 2015) (Table DR1), and were opened, macro- and microscopically described, imaged and logged with a Geotek multi-sensor core logger (MSCL) at a down-core step-size of 2 mm (Bartington MS2E point sensor for magnetic susceptibility (MS) and Konica Minolta spectrophotometer for reflectance spectroscopy) at Ghent University. For each data point, the visible-light (360-740 nm) reflectance spectrum was obtained at 10 nm intervals with a half bandwidth of ~10 nm. The R_{560}/R_{665} reflectance ratio was calculated by dividing the average of R_{550}, R_{560} and R_{570} by that of R_{660} and R_{670}, in order to mimic the bandwidths obtained from the satellite reflectance data (see further), and thereby obtain comparable R_{560}/R_{665} reflectance ratios. Most (13) cores were scanned with a Siemens Somatom Definition Flash medical X-ray computed tomography (CT) scanner at the Ghent University Hospital, which was employed at 120 kV, an effective mAs of 200 and a pitch of 0.45. Reconstructed volumes have a voxel size of 0.15x0.15x0.6 mm (2011 and 2012) or 0.15x0.15x0.3 mm (2015). In the master core (i.e. ENC12-03), the sampling procedure for laser-diffraction grain-size analysis of the clastic fraction was as follows: turbidites were contiguously sampled at 3 mm intervals and in laminated hemipelagic mud 3 mm wide samples were retrieved at ~1 cm intervals. Samples were treated with boiling H_20_2 and HCl for removal of organic matter and carbonates, respectively, before being analyzed with a Malvern Mastersizer 3000 (see also Van Daele et al., 2016). Throughout the master core, organic-matter content was estimated for 35 samples using loss-on-ignition (Heiri et al., 2001). Core ENC12-04 (i.e. a replica of master core ENC12-03) was scanned with a Itrax XRF core scanner at a resolution of 1 mm at the University of Innsbruck. The XRF scanner was employed at 30kV and 45 mA, and using a 5 s exposure time. Reproducibility was shown by executing duplicate tests.

Table DR1: core locations and sampling periods.

Core name	Month	Year	Lat (°N)	Long (°E)
ENC11-01	January	2011	-33.6706	-70.1345
ENC11-02	January	2011	-33.6721	-70.1332
ENC12-03	February	2012	-33.6724	-70.1330
ENC12-04	February	2012	-33.6724	-70.1330
ENC12-05	February	2012	-33.6723	-70.1342
ENC12-06	February	2012	-33.6708	-70.1350
ENC12-07	February	2012	-33.6703	-70.1336
ENC12-08	February	2012	-33.6698	-70.1322
ENC12-09	February	2012	-33.6724	-70.1314
ENC15-01	December	2015	-33.6717	-70.1334
ENC15-02	December	2015	-33.6712	-70.1324
ENC15-03	December	2015	-33.6705	-70.1342
ENC15-04	December	2015	-33.6711	-70.1342
ENC15-05	December	2015	-33.6684	-70.1330
ENC15-06	December	2015	-33.6734	-70.1325
ENC15-07	December	2015	-33.6722	-70.1330

The selected master core (ENC12-03) is located at the southern edge of the depocenter, but in the middle of the area showing least acoustic reflectivity on the side-scan sonar data. The low reflectivity indicates presence soft, muddy sediments, compared to more sandy sediments on the proximal locations. As these sands occur in the base of the turbidites, and are an indication

of higher-energy flow regimes, their presence increases the chance of erosion by the currents. The low-reflectivity zone (from which the master core is retrieved) thus indicates the area in the lake with minimal chance of erosional surfaces.

Chronology

A first order chronology of master core ENC12-03 was established by analyzing ^{137}Cs-, ^{210}Pb-, ^{226}Ra-, and ^{232}Th-activities of freeze-dried samples. These were measured by gamma spectrometry with a low-background, high-efficiency well-type germanium detector equipped with a Cryo-Cycle (CANBERRA) (Schmidt and De Deckker, 2015) at the University of Bordeaux. In order to reduce impact of changes in sediment composition and grain size, excess lead (^{210}Pb$_{xs}$; unsupported by its parent isotope ^{226}Ra) was normalized for ^{232}Th activity (Stupar et al., 2014). In order to calculate an accurate age model two transformations were performed to the depth scale: (i) the turbidites with a thickness ≥0.8 cm were excluded, resulting in a "corrected depth", and (ii) a power fit through weights of 26 freeze-dried samples of a similar volume (spread throughout the core) allowed to convert the corrected depth (cm) to cumulative dry mass deposition (g/cm²) (e.g., Stupar et al., 2014). The second step was executed to reduce the influence of the higher water content in the upper centimeters, which significantly increases the apparent sedimentation rate. Depositional ages were estimated using a Constant Flux - Constant Sedimentation (CF-CS) model (Oldfield and Appleby, 1984) (Fig. DR1). The error on the slope of the model fit was used to produce a Gaussian probability density function for each turbidite (Fig. 2), minimum and maximum ages (Table DR3) are based on a 1 standard deviation error. The ^{137}Cs profile was used to estimate the depth of (i) the southern hemisphere ^{137}Cs peak fallout in 1964 (i.e. 1964.0 – 1965.0) (Hancock et al., 2014) and (ii) the first widely detectable ^{137}Cs fallout around 1954 (Hancock et al., 2014; UNSCEAR, 2000), both supporting the ^{210}Pb$_{xs}$ age model – as the "best ages" of the latter are within a year of the expected age based on literature –, but also confining some of the event dates (Fig. 2, DR1; Table DR2).

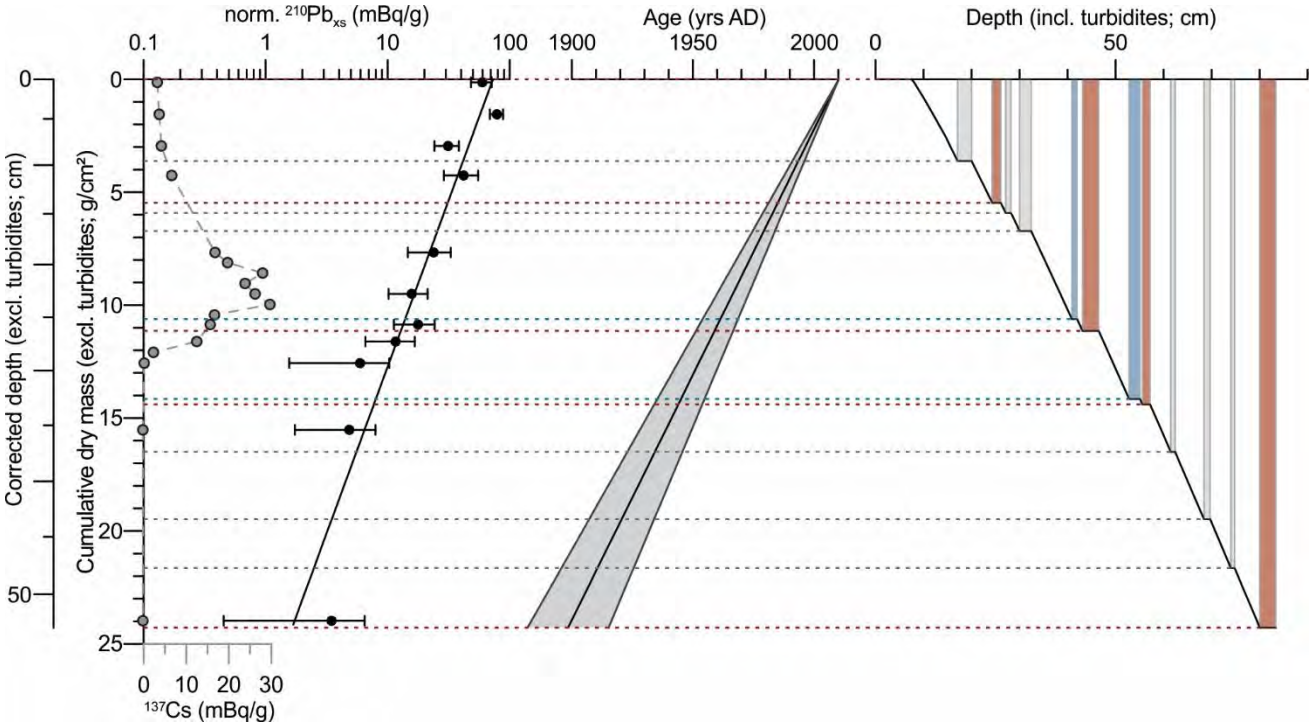

Figure DR1: Radionuclide age model for core ENC12-03 against cumulative dry mass (and corrected depth for reference). From left to right: ^{137}Cs activity, ^{210}Pb$_{xs}$ normalized using ^{232}Th activity, CF-CS age model based on normalized ^{210}Pb$_{xs}$, with an uncertainty of 1 standard deviation; relation to depth with indication of turbidites, which were excluded from the age model. Turbidite colors indicate their class: C1 (red), C2a (grey) and C2b (blue), see also Figure 2 and DR2.

In the lower half of the record, a floating varve chronology was constructed. Four independent counters (authors MVD, IM, PK and JM) counted each three times on the CT images using the ImageJ software (Schneider et al., 2012). Taking into account that the varve year of these clastic varves starts in October (strong rise in river discharge due to spring melt), and that fallout records are based on calendar years, two varves are a candidate to contain the onset of ^{137}Cs fallout in 1954, which can thus serve as a tie-point for the floating varve chronology. As all 12 countings were tied to each 1954 candidate, a total of 24 countings were used to calculate an average varve model as well as a Gaussian probability density function for each turbidite. Minimum and maximum ages (Table DR2) are based on a 1 standard deviation error. The varve model is supported by the $^{210}Pb_{xs}$ age model, as the latter completely encloses the varve model, which has a much higher accuracy (Fig. 2). The increasing offset between the model averages in the first 2 decades of the 20th century is a result of the higher sedimentation rate, which cannot be accommodated by the CF-CS model. The final age-depth model is a combination of the $^{210}Pb_{xs}$ model (1958.9 – 2010.2) and the varve model (1905.7 – 1958.9).

Table DR2: Best, minimum and maximum ages for each turbidite based $^{210}Pb_{xs}$ and varve chronology. First occurrence and peak ^{137}Cs fallout provide minimum and maximum ages. For the combined age model, the combination of minimum and maximum ages resulting in the narrowest range was retained, as well as the associated "best" age.

		$^{210}Pb_{xs}$ (yrs AD)			^{137}Cs (yrs AD)		Varve counting (yrs AD)			Combined (yrs AD)			Correlated historical event		Offset
Name	Type	Min	Best	Max	Min	Max	Min	Best	Max	Min	Best	Max	Date	Description	(yrs)
T1	C1												2010.2	co-seismic	
T2	C2a	1996.0	1993.5	1991.0	2010.2	1964.5	-	-	1957.5	1996.0	1993.5	1991.0	1993.4	snowmelt event	-0.12
T3	C1	1988.7	1985.0	1981.2	2010.2	1964.5	-	-	1957.5	1988.7	1985.0	1981.2	1985.2	co-seismic	0.19
T4	C2a	1987.0	1983.0	1978.9	2010.2	1964.5	-	-	1957.5	1987.0	1983.0	1978.9	1983.0	summer rainfall	0.05
T5	C2a	1983.9	1979.3	1974.6	2010.2	1964.5	-	-	1957.5	1983.9	1979.3	1974.6	1979.0	summer rainfall	-0.26
T6	C2b	1968.6	1961.3	1954.0	1964.5	1954.0	-	-	1957.5	1964.5	1961.3	1957.5	?	post-seismic	
T7	C1	1966.6	1958.9	1951.2	1964.5	1954.0	1960.3	1958.9	1957.5	1960.3	1958.9	1957.5	1958.7	co-seismic	-0.20
T8	C2b	1954.8	1945.0	1935.3	1954.0	-	1947.5	1946.4	1945.2	1947.5	1946.4	1945.2	?	post-seismic	
T9	C1	1953.8	1943.9	1934.0	1954.0	-	1946.5	1945.4	1944.2	1946.5	1945.4	1944.2	1945.7	co-seismic	0.34
T10	C2a	1945.6	1934.3	1922.9	1954.0	-	1936.7	1934.4	1932.1	1936.7	1934.4	1932.1	1935.0	summer rainfall	0.60
T11	C2a	1934.0	1920.6	1907.1	1954.0	-	1926.3	1923.1	1920.0	1926.3	1923.1	1920.0	?	?	
T12	C2a	1925.5	1910.6	1895.7	1954.0	-	1919.5	1916.1	1912.6	1919.5	1916.1	1912.6	1917.0	building aqueduct	0.95
T13	C1	1915.2	1898.4	1881.7	1954.0	-	1909.8	1905.7	1901.6	1909.8	1905.7	1901.6	1906.6	co-seismic	0.91

River discharge data

River discharge data presented in Figure 2 was compiled from two stations on the Maipo River downstream of Lo Encañado Lake: station El Ingenio (1913-1940) and El Manzano (1947-2016). Data was obtained from the Dirección de General de Aguas (DGA, Chilean Government).

Intensity calculations

To determine Modified Mercalli Intensities (MMI) of historical earthquakes at the lake, we used intensity prediction equations (IPEs) depending on the source fault (Table DR3) (see also Moernaut et al., 2014).

- For megathrust earthquakes we used the relationship of Barrientos (1980), based on a compilation of primarily Chilean megathrust earthquakes,

$$MMI = 1.3844\ Ms - 3.7355\ \mathrm{Log}^{10}(D) - 0.0006\ D + 3.91,$$

where *Ms* is surface-wave magnitude, and *D* is the estimated distance to the main asperity as suggested by Astroza et al. (2012);

- For intraslab earthquakes we used relationships that were established for the specific earthquakes by Astroza et al. (2005),

$$MMI = 20.357 - 7.122\ \mathrm{Log}^{10}(D) + 0.0017\ D \text{ (Santiago 1945 } Ms\text{=7.1)},$$
$$MMI = 28.364 - 10.200\ \mathrm{Log}^{10}(D) + 0.0047\ D \text{ (La Ligua 1965 } Ms\text{=7.1/7.5)},$$

where *D* is hypocentral distance. For the 1942 Ms=6.9 intraslab earthquake we used the Santiago 1945 Ms=7.1 attenuation relationship, which provides an upper intensity limit;

- For the 1958 crustal earthquake we used the relationship that Bakun and Wentworth (1997) developed for Californian earthquakes,

$$MMI = 5.07 + 1.09\ Mw - 3.69\ \mathrm{Log}^{10}(Dh),$$

where *Mw* is moment magnitude and *Dh* is epicentral distance. For the 1958 earthquake this attenuation relationship provides a very good fit with the reported intensity data (Sepulveda et al., 2008), when using an M_w=6.3 (Alvarado et al., 2009).

Table DR3: Source parameters and selected IPEs for historical earthquakes in central Chile (Alvarado et al., 2009; Astroza et al., 2005; Comte et al., 1986; SISRA, 1985; USGS, 2010). Dh: horizontal distance, i.e. (i) epicentral distance when using Bakun and Wentworth (1997) and Astroza et al. (2005) attenuation relationships and (ii) arbitrary distance to main asperity when using the Barrientos (1980) attenuation relationship; Dv: vertical distance or depth; D: distance based on Dh and Dv. When different magnitudes are published, the average was used to calculate the MMI at Lo Encañado Lake.

Year	Month	Day	Days	Age (dec.)	M_s	M_w	Dh (km)	Dv (km)	D (km)	MMI	Data sources	Attenuation relationship
1906	Aug	16	228	1906.62	8.3	8.2	170	30	173	6.9	SISRA (1985); Comte et al. (1986)	Barrientos (1980)
1928	Dec	1	335	1928.92	8.0/8.2	-	300	30	301	5.7	SISRA (1985); Comte et al. (1986)	Barrientos (1980)
1942	Jun	29	180	1942.49	6.9	-	110	100	149	5.1	SISRA (1985)	Astroza et al. (2005)
1943	Apr	6	96	1943.26	7.9	8.2	280	30	282	5.5	SISRA (1985); Comte et al. (1986)	Barrientos (1980)
1945	Sep	13	256	1945.70	7.1	7.1	35	90	97	6.4	SISRA (1985); Astroza et al. (2005)	Astroza et al. (2005)
1958	Sep	4	247	1958.68	5.7	6.3	20	8	22	7.1	SISRA (1985); Alvarado et al. (2009)	Bakun and Wentworth (1997)
1960	May	22	142	1960.39	8.5	9.5	560	30	561	5.1	SISRA (1985)	Barrientos (1980)
1965	Mar	28	87	1965.24	7.1/7.5	-	175	70	188	6.0	SISRA (1985); Astroza et al. (2005)	Astroza et al. (2005)
1971	Jul	9	190	1971.52	7.5/7.9	7.8	200	30	202	5.8	SISRA (1985); Comte et al. (1986)	Barrientos (1980)
1985	Mar	3	62	1985.17	7.8	8	170	30	173	6.2	Comte et al. (1986)	Barrientos (1980)
2010	Feb	27	58	2010.16	8.5	8.8	230	30	232	6.7	USGS (2010)	Barrientos (1980)

Computation of acceleration response spectra

We downloaded accelerograms recorded in four stations (with codes FAR1, MT02, MT05 and VA05) of the Chilean National Seismological Center (CSN) for the M=6.9 megathrust earthquake of 24 April 2017 (http://evtdb.csn.uchile.cl/event/0565d07e6e3c0e823e8e32c18687eba8) and the M=5.5 intraslab earthquake of 2 August 2017 (http://evtdb.csn.uchile.cl/event/ 0565d07e75906739a7e44d936e89930a). For each station and event, we isolated the S wave, rotated the horizontal components to radial and transverse components, and detrended the signal. We then computed acceleration response spectra (5% damping) for the SH wave on the transverse component in the frequency domain using the complex frequency response function, representing the steady-state response of a single-degree of freedom oscillator to harmonic excitation of its support (e.g., Gavin, 2016).

Modeling of response spectra for megathrust and intraslab earthquakes

The frequency content of ground motion at a given site depends on many variables, including the type of earthquake (megathrust, intraslab or crustal), magnitude, hypocentral depth, distance between source and site, the path and other variables. In order to better understand in which magnitude and distance ranges response spectra of typical megathrust and intraslab earthquakes can be distinguished at the Andean station FAR1 (and hence in Andean lakes in general), we modeled response spectra using the ground-motion prediction equation (GMPE) of Idini et al. (2017), which has different functional forms for subduction interface (megathrust) and intraslab earthquakes, and is based on data from the Chilean subduction zone.

Satellite reflectance data

Surface characteristics in the catchment were analyzed at a 10 m resolution using reflectance bands B03 (green, 560 nm, 35 nm bandwidth) and B04 (red, 665 nm, 30 nm bandwidth) obtained by Sentinel 2. We used the ESA Sentinel Application Platform (SNAP) to produce the B03/B04 ratio, which was then compared to the corresponding ratio (with a similar bandwidth) obtained from the reflectance spectroscopy on the sediment core (Fig. 3e,f).

RESULTS

Stratigraphy

Hemipelagic sediments

The change in composition of the laminated sediment throughout the 20th century can be primarily attributed to anthropogenic impact. While in the first decades of the 20th century hemipelagic sediments are dominated by siliciclastic material forming clastic varves (after Zolitschka et al., 2015), the sediments become gradually more organic between 1920 and 1960, resulting in increasingly blurry laminations. This change in sedimentation (rate) is especially clear in core ENC15-05 (Fig. DR2), located near the inflow sourcing from the upstream located Negra Lake (Fig. 1). We therefore attribute the change in sedimentation pattern to the commissioning of an aqueduct draining Negra Lake (Fig. 1) in 1917, thereby increasingly bypassing Lo Encañado Lake and causing a decreasing water flux through the lake, which nearly completely ceased halfway the 20th century (after the population explosion of Santiago).

C2 turbidites

All C2 turbidites (i.e. C2a and C2b) can be considered flood turbidites, in which the production of a deposit depends on (i) high discharge due to intense rainfall or snowmelt and (ii) available "loose" material in the catchment. While C2a turbidites are related to a drastic increase of the former (discharge), C2b turbidites are mainly triggered by an increase of the latter (available material), but will also require a considerable discharge increase.

C2a turbidites

All the prominent C2a turbidites can be linked to historical flooding and anthropogenic impact (Table DR2). The turbidite T12, which was dated to 1916.1, is attributed to the impact of the construction of the aqueduct at Negra Lake. The ~1979.3 and ~1983.0 turbidites (T5 and T4) are attributed to increased summer rainfall in 1978-79 and 1982-83, although the latter may also be related to the winter flood conditions reported in Santiago de Chile (http://repositoriodigitalonemi.cl/web/handle/2012/). The ~1993.5 turbidite (T2) is triggered by a flood event caused by heavy autumn rainfall and snowmelt resulting from a rise of the 0°C isotherm on the 3rd of May 1993 (OCHA, 1993; ONEMI, 1993). The turbidites thus seem to be triggered by short-lived, but extreme events which may or may not show up in monthly averaged discharge data. The 2011 turbidite (T0) likely results from constructions related to the Alto Maipo Hydroelectric project (http://www.altomaipo.com).

These correlations of the sedimentary deposits to historical flooding and anthropogenic activities all support the combined varve-radionuclide age model.

C2b turbidites, and their relation to C1 turbidites

While the C2b turbidite that is related to the 1945 earthquake (T8) occurs immediately above the C1 turbidite triggered by this earthquake (T9), this is not the case for the C2b turbidite (T6) following the 1958 C1 turbidite (T7). The latter are separated by 1-1.5 cm of hemipelagic sediments and the C2b turbidite has an age of 1961.3 (Table DR2), which corresponds to a 2.4 year delay compared to the C1 turbidite. The timing of T6 coincides with the start of a period of moderate discharge maxima around 1961 and thus seems to be related to weather conditions as well. Nevertheless, even though C2b turbidites are depending on the occurrence of (weak) flood conditions, they are still genetically linked to C1 turbidites triggered by intraplate earthquakes. The probability that during a 109 year period, the only two C2b turbidites would occur by chance within a 3 year window after the only two intraplate earthquakes causing strong shaking (i.e. MMI>VI), is as low as 0.15%, and 0.42% when we consider a 5 year window. Hence, it is highly unlikely that the relation between the intraplate earthquakes and the C2b turbidites is by chance.

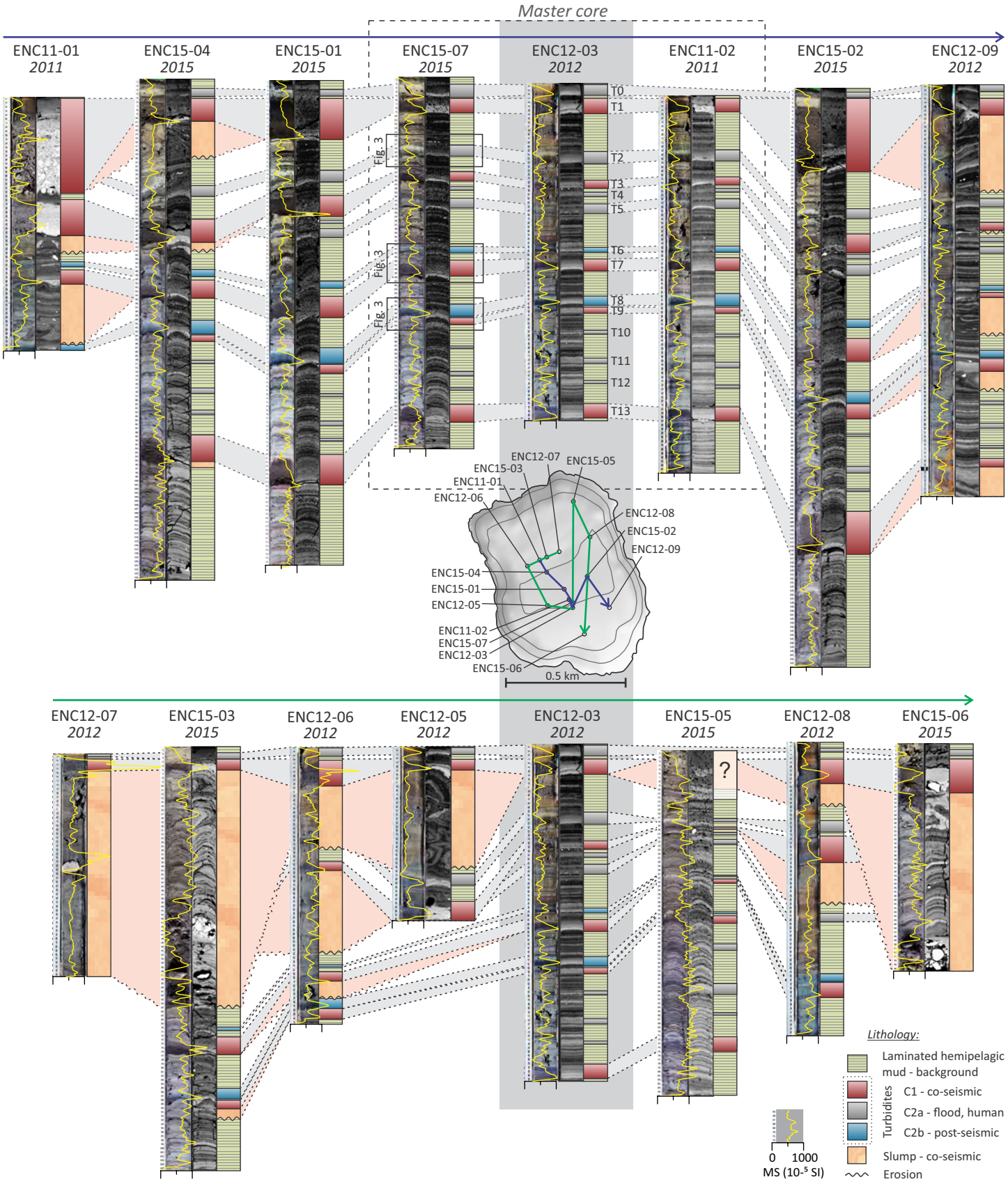

Figure DR2: Correlation of all short cores to master core ENC12-03 along two arbitrary transects as indicated on the map (isobaths every 10 m). The upper transect (blue) contains predominantly cores with a complete record (no erosion) from the central part of the lake. The lower transect (green) contains most cores from near-slope environments, with frequent erosional slumps. Each core is presented by (from left to right): histogram equalized core image with magnetic susceptibility (MS, yellow line), CT scan view along core surface (for most cores) and lithology.

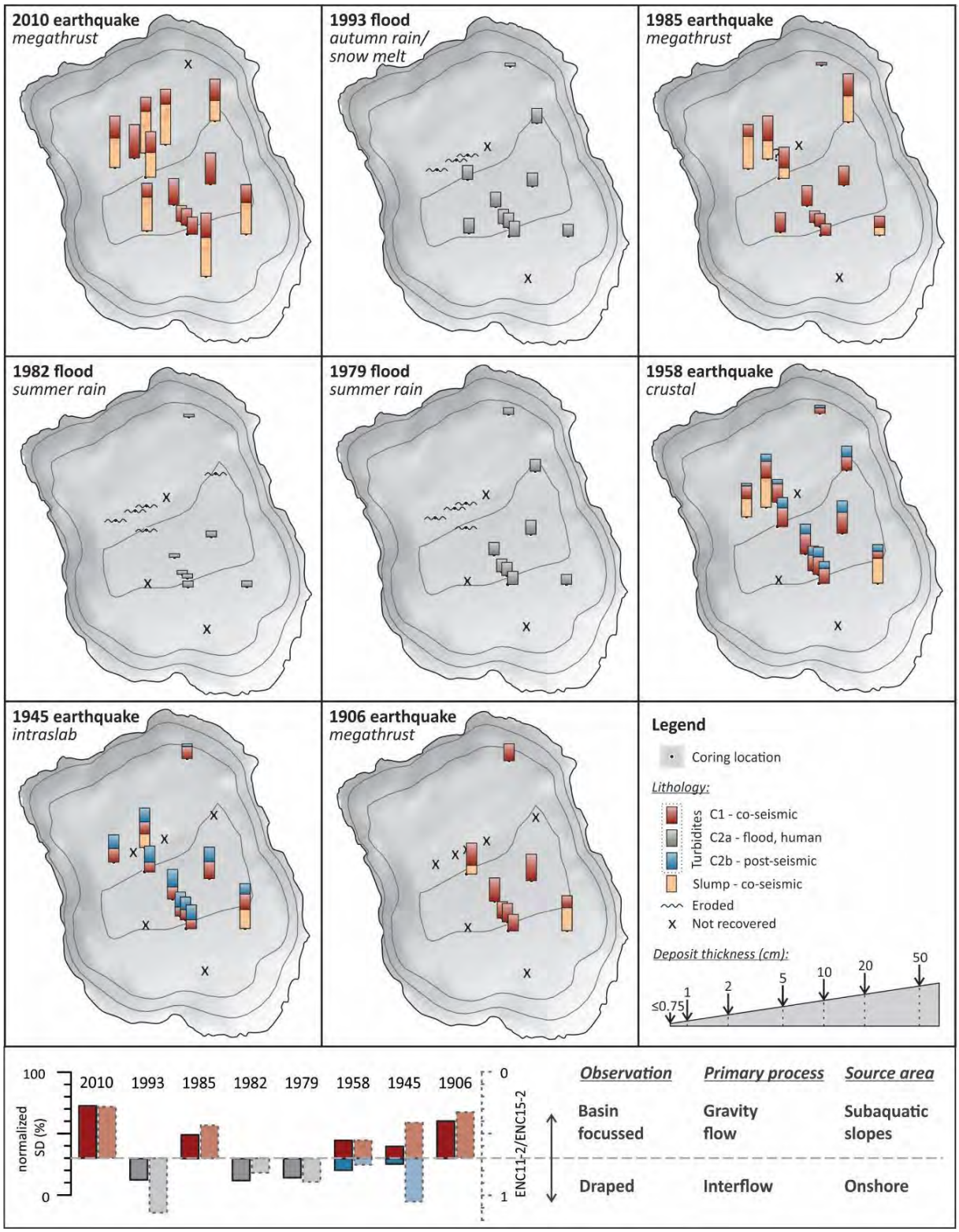

Figure DR3: top: distributions and sequences of the deposits (slumps and turbidites) triggered by the 8 main events recoded in the Lo Encañado sediments since 1900 AD. Thickness of single deposits can be derived from the triangle in the lower right box. Isobaths every 10 m. Bottom: normalized standard deviation (SD) of turbidite thickness (dark/bright colors) as derived from the 6 cores that contain each turbidite (i.e. ENC11-02, ENC12-03, ENC12-09, ENC15-01, ENC15-02 and ENC15-07), and ratio of turbidite thickness at the lower slope (ENC11-02) to that at the depocenter (ENC15-02). High values in both variables indicated a basin-focused geometry of the deposit, while low values are indicative for draping.

Reflectance spectroscopy

The relatively blue color of the C2b turbidites (Fig. 3) is shown in the reflectance spectra by the relatively high reflection of light with wavelengths of ~450 to ~550 nm – representing blue to green light – compared to that of the other sediments. These higher reflections in the 450-550 nm range can be attributed to (a combination of) several factors:

(i) Absence of carotenoid pigments, which occur in degraded organic matter, but not in mineroclastics. They typically absorb blue light with wavelengths between 460 and 510 nm. Blue light is thus more absorbed (and less reflected) in organic rich sediments and turbidites, and less absorbed (and more reflected) in clastic-rich turbidites.

(ii) Presence of mineroclastics, and especially chlorites such as clinochlore, which are omnipresent in the catchment (Robinson et al., 2004). They typically reflect blue-green light (500-550 nm) well, while they absorb red light (~700 nm) (Kokaly et al., 2017). Fresh (unweathered) mineroclastics will thus more efficiently reflect blue light compared to red light.

(iii) Absence of iron oxides, which are likely present in weathered rocks and soils, giving them their reddish color (Fig. 3). Iron oxides typically reflect red light (>700 nm) very well, while they absorb nearly all blue and green light (<500 nm) (Kokaly et al., 2017). Weathered iron-bearing mineroclastics, typically containing iron oxides, will thus absorb the blue light, resulting in a relatively blue color for their unweathered counterparts.

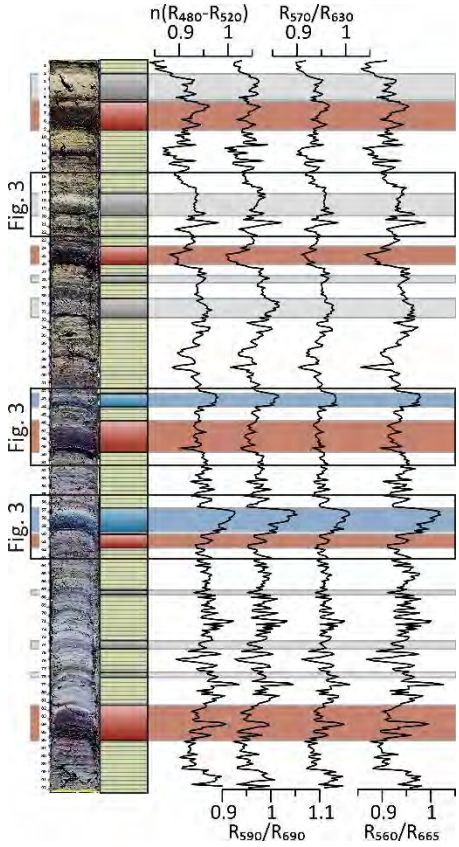

These relatively high reflections in the 450-550 nm range (peaking around 500 nm) is clearly illustrated by the average reflectance between 480 and 520 nm normalized for mean reflectance (i.e. $n(R_{480}\text{-}R_{520})$)(Fig. DR4). However, in literature the slope gradient on the side of the longer wavelengths has often been used. Trachsel et al. (2010) use R_{590}/R_{690} to quantify amount of a.o. chlorite, while Rein and Sirocko (2002) use R_{570}/R_{630} to quantify the amount of mineroclastics compared to organic matter. In order to compare our sediment reflectance data with that of Sentinel 2 satellite reflectance data of the catchment, we use R_{560}/R_{665}, as these are the reflectance bands available from the remote sensing data that best resemble the published ones (Fig. DR4).

Figure DR4: Color reflectance data from core ENC15-07. From left to right: processed core image, lithology, average reflectance between 480 and 520 nm normalized for mean reflectance ($n(R_{480}\text{-}R_{520})$), ratio of reflectance at 590 nm to 690 nm (R_{590}/R_{690}) after Trachsel et al. (2010), ratio of reflectance at 570 nm to 630 nm (R_{570}/R_{630}) after Rein and Sirocko (2002), ratio of reflectance at 560 nm to 665 nm (R_{560}/R_{665}) mimicking the bandwidths obtained from the satellite reflectance data, i.e. 35 and 30 nm, respectively.

Acceleration response spectra

Figure DR5 shows acceleration response spectra computed for two recent earthquakes, one megathrust and one intraslab, in four stations, arranged more or less along a line from the coast to the Andes. In each station, the spectral acceleration (SA) peaks at higher frequencies (shorter periods) for the intraslab earthquake than for the megathrust earthquake, but this is most evident at the Andean station FAR1, where maximum SAs are similar for both earthquakes.

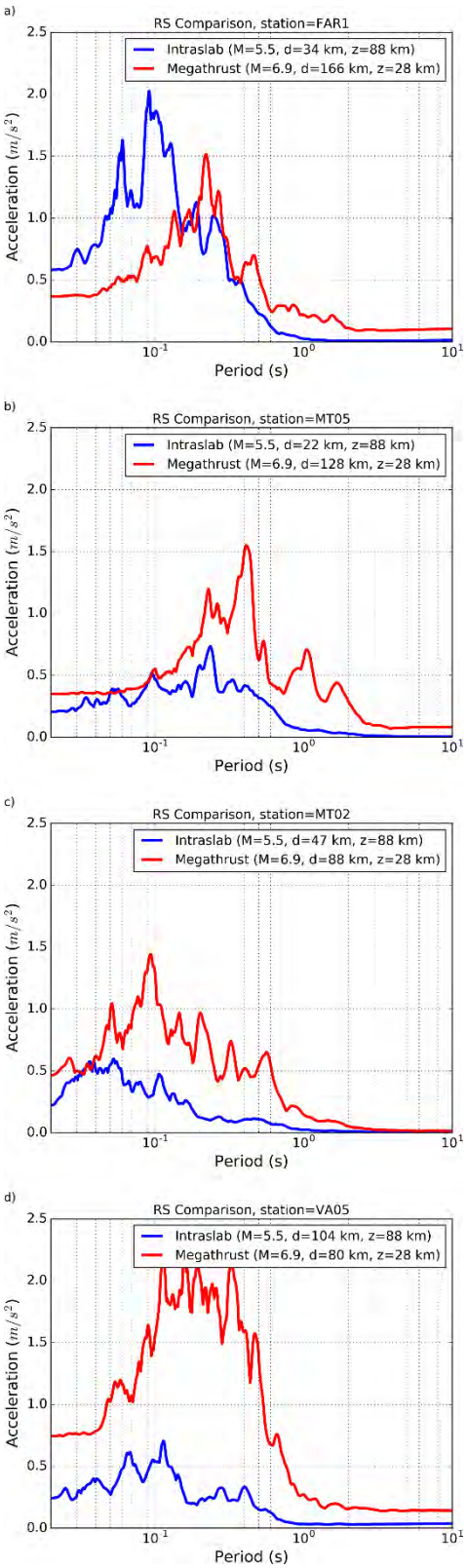

Figure DR5: Acceleration response spectra (5% damping) along a longitudinal transect of four seismic stations (location: Fig. 1a) for the 2017 intraslab (blue) and megathrust (red) earthquakes.

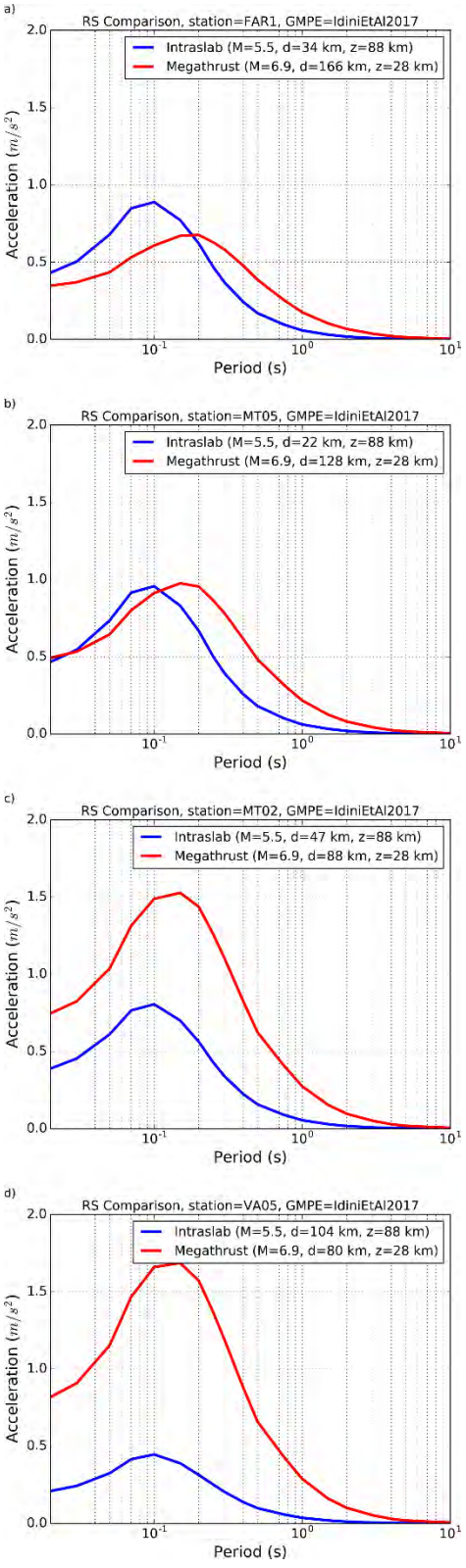

Figure DR6: Response spectra (5% damping) modelled using the GMPE of Idini et al. (2017) for the 2017 intraslab (blue) and megathrust (red) earthquakes in the same stations as Figure DR5.

Modeled response spectra for megathrust and intraslab earthquakes

We first compared the response spectra modelled using the GMPE of Idini et al. (2017) for rock sites (Fig. DR6) with those computed from accelerograms of the two recent megathrust and intraslab events in all four stations (Fig. DR5). Although the match is not perfect, the relative shapes and peak heights of modelled and observed response spectra are in good agreement, confirming that the GMPE is representative of our particular situation. Differences in amplitude may be explained by differences in the selected horizontal component (not reported in Idini et al. (2017)), site effects, and natural ground-motion variability.

Subsequently, we modelled response spectra at station FAR1 for megathrust and intraslab earthquakes with different magnitudes and/or distances. We used fixed hypocentral depths of 35 and 100 km, respectively, and considered a fixed horizontal distance for megathrust earthquakes (170 km, similar to the 24 April 2017 earthquake, and more or less corresponding to the distance to the edge of the subduction interface). In Figure DR7, we evaluate the effect of magnitude. Figure DR7A shows response spectra for intraslab earthquakes at a distance of 34 km (similar to the 2 August 2017 earthquake) and with magnitudes varying between M=5.0 and M=6.5, compared to the response spectrum for an M=7.0 megathrust earthquake. These show that intraslab earthquakes with magnitudes up to one unit lower than a megathrust earthquake generate distinctively larger accelerations at high frequency ($T < 0.2$ s or $f > 5$ Hz). Conversely, Figure DR7b demonstrates that megathrust earthquakes with magnitudes of at least one unit larger than an intraslab earthquake at the same distance generate significantly larger accelerations at low frequency. In Figure DR8, we compare response spectra for megathrust and intraslab earthquakes of the same magnitude (M=7.0), varying the horizontal distance of the intraslab earthquake between 10 and 200 km. It is again obvious that at distances that are shorter than the distance to a comparable megathrust earthquake, intraslab earthquakes generate distinctively larger accelerations at high frequency.

The modelled response spectra support our hypothesis that Lo Encañado Lake is located at the right distance from the megathrust to be more sensitive to high-frequency accelerations from intraslab earthquakes than from megathrust earthquakes with magnitudes up to one unit higher and at comparable or longer distances.

We also compared response spectra of historical earthquakes (1945, 1985 and 2010) with Chiapas-like earthquakes (M_w 8.2, Mexico 2017) – as an equivalent for the strongest plausible intraslab earthquake – at varying distances (10 – 200 km) (Fig. DR9). This shows that a large intraslab earthquake at a large distance still produces larger accelerations at high frequencies compared to megathrust earthquakes.

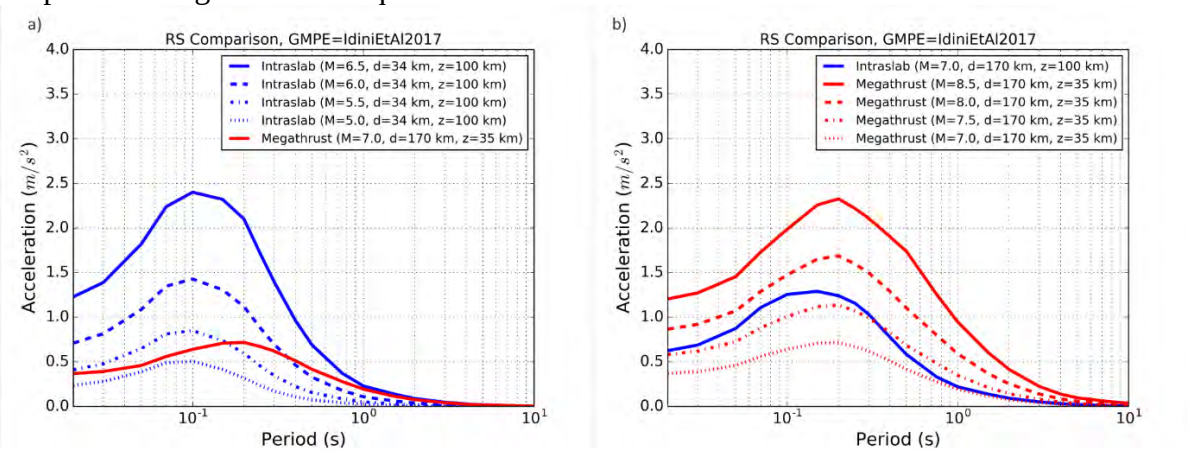

Figure DR7: Evaluation of effect of magnitude on response spectra (5% damping) modelled with the Idini et al. (2017) GMPE for intraslab (blue) and megathrust (red) earthquakes. A) intraslab earthquakes with magnitudes between M=5.0 and M=6.5 at a horizontal distance of 34 km versus M=7.0 megathrust earthquake at 170 km distance; B) megathrust earthquakes with magnitudes between M=7.0 and M=8.5 versus M=7.0 intraslab earthquake, all at a horizontal distance of 170 km.

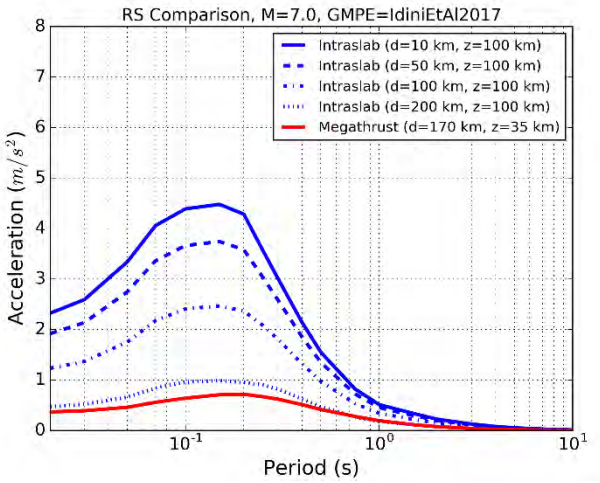

Figure DR8: Comparison of response spectra (5% damping) modelled with the Idini et al. (2017) GMPE for M=7.0 intraslab earthquakes (blue) at varying horizontal distances (10 – 200 km) and megathrust earthquake (red) with same magnitude at fixed distance (170 km).

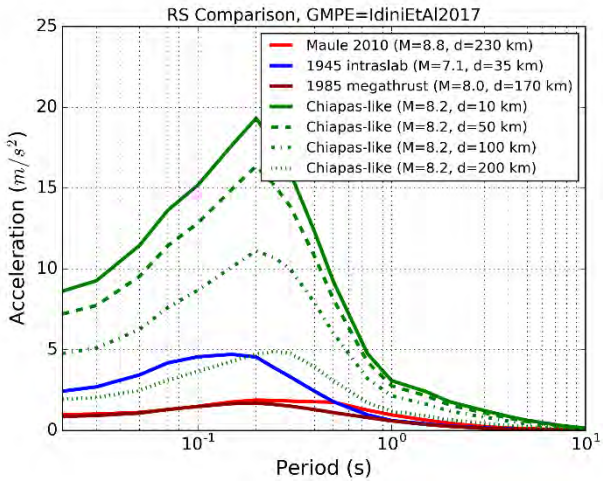

Figure DR9: Comparison of response spectra (5% damping) at Lo Encañado Lake, modelled with the Idini et al. (2017) GMPE for the historical 1945 (blue), 1985 (brown) and 2010 (red) earthquakes, and a Chiapas-like intraslab earthquake at varying horizontal distances (10 – 200 km) (green).

REFERENCES CITED

Alvarado, P., Barrientos, S., Saez, M., Astroza, M., and Beck, S., 2009, Source study and tectonic implications of the historic 1958 Las Melosas crustal earthquake, Chile, compared to earthquake damage: Physics of the Earth and Planetary Interiors, v. 175, no. 1-2, p. 26-36

Astroza, M., Ruiz, S., and Astroza, R., 2012, Damage Assessment and Seismic Intensity Analysis of the 2010 (Mw 8.8) Maule Earthquake: Earthquake Spectra, v. 28, no. S1, p. S145-S164. doi: 10.1193/1.4000027

Astroza, M., Sandoval, H., and Kausel, E., 2005, Estudio comparativo de los effectos de los sismos Chilenos de subducción del tipo intraplaca de profundidad intermedia, Congreso Chileno de Sismología e ingeniaría Antisísmica: Concepción, Chile.

Bakun, W. H., and Wentworth, C. M., 1997, Estimating earthquake location and magnitude from seismic intensity data: Bulletin of the Seismological Society of America, v. 87, no. 6, p. 1502-1521

Barrientos, S., 1980, Regionalización sísmica de Chile [MSc thesis]: Universidad de Chile, 72 p.

Comte, D., Eisenberg, A., Lorca, E., Pardo, M., Ponce, L., Saragoni, R., Singh, S. K., and Suarez, G., 1986, The 1985 Central Chile Earthquake: A Repeat of Previous Great Earthquakes in the Region?: Science, v. 233, no. 4762, p. 449-453. doi: 10.1126/science.233.4762.449

Gavin, H. P., 2016, Vibrations of Single Degree of Freedom Systems. Lecture notes of course CEE 541 Structural Dynamics, Department of Civil and Environmental Engineering, Duke University, p. 39.

Hancock, G. J., Tims, S. G., Fifield, L. K., and Webster, I. T., 2014, The release and persistence of radioactive anthropogenic nuclides: Geological Society, London, Special Publications, v. 395, no. 1, p. 265-281. doi: 10.1144/sp395.15

Heiri, O., Lotter, A. F., and Lemcke, G., 2001, Loss on ignition as a method for estimating organic and carbonate content in sediments: reproducibility and comparability of results: Journal of Paleolimnology, v. 25, no. 1, p. 101-110

Idini, B., Rojas, F., Ruiz, S., and Pastén, C., 2017, Ground motion prediction equations for the Chilean subduction zone: Bulletin of Earthquake Engineering, v. 15, no. 5, p. 1853-1880. doi: 10.1007/s10518-016-0050-1

Kokaly, R. F., et al., 2017, USGS Spectral Library Version 7, 1035. http://pubs.er.usgs.gov/publication/ds1035 (accessed October 2018)

Moernaut, J., Van Daele, M., Heirman, K., Fontijn, K., Strasser, M., Pino, M., Urrutia, R., and De Batist, M., 2014, Lacustrine turbidites as a tool for quantitative earthquake reconstruction: New evidence for a variable rupture mode in south central Chile: Journal of Geophysical Research: Solid Earth, v. 119, p. 1607-1633. doi: 10.1002/2013JB010738

OCHA (UN Office for the Coordination of Humanitarian Affairs), 1993, Chile Mudslides/Floods May 1993 UNDHA Information Reports 1 - 2. https://reliefweb.int/report/chile/chile-mudslidesfloods-may-1993-undha-information-reports-1-2 (accessed February 2018)

Oldfield, F., and Appleby, P. G., 1984, Empirical testing of Pb-210-dating models for lake-sediments, *in* Haworth, E. Y., and Lund, J. G., eds., Lake Sediments and Environmental History: Leicester, Leicester University Press, p. 93–124.

ONEMI (Ministerio del Interior y Seguridad Pública - Gobierno de Chile), 1993, Informe de situación - Catastrofe provocada por lluvias a contar del lunes 3 de Mayo de 1993. (accessed February 2018)

Rein, B., and Sirocko, F., 2002, In-situ reflectance spectroscopy - analysing techniques for high-resolution pigment logging in sediment cores: International Journal of Earth Sciences, v. 91, no. 5, p. 950-954. doi: DOI 10.1007/s00531-002-0264-0

Robinson, D., Bevins, R. E., Aguirre, L., and Vergara, M., 2004, A reappraisal of episodic burial metamorphism in the Andes of central Chile: Contributions to Mineralogy and Petrology, v. 146, no. 4, p. 513-528. doi: 10.1007/s00410-003-0516-4

Schmidt, S., and De Deckker, P., 2015, Present-day sedimentation rates on the southern and southeastern Australian continental margins: Australian Journal of Earth Sciences, v. 62, no. 2, p. 143-150. doi: 10.1080/08120099.2015.1014846

Schneider, C. A., Rasband, W. S., and Eliceiri, K. W., 2012, NIH Image to ImageJ: 25 years of image analysis: Nature Methods, v. 9, no. 7, p. 671-675. doi: 10.1038/nmeth.2089

Sepulveda, S. A., Astroza, M., Kausel, E., Campos, J., Casas, E. A., Rebolledo, S., and Verdugo, R., 2008, New Findings on the 1958 Las Melosas Earthquake Sequence, Central Chile: Implications for Seismic Hazard Related to Shallow Crustal Earthquakes in Subduction Zones: Journal of Earthquake Engineering, v. 12, no. 3, p. 432-455. doi: 10.1080/13632460701512951

SISRA, 1985, Hypocenter data, *in* Askew, B. L., and Algermissen, S. T., eds., Catalog of earthquakes for South America, Volume 5: Lima, Peru, Centro Regional de Sismología para América del Sur (CERESIS), p. 125.

Stupar, Y. V., Schäfer, J., García, M. G., Schmidt, S., Piovano, E., Blanc, G., Huneau, F., and Le Coustumer, P., 2014, Historical mercury trends recorded in sediments from the Laguna del Plata, Córdoba, Argentina: Chemie der Erde - Geochemistry, v. 74, no. 3, p. 353-363. doi: 10.1016/j.chemer.2013.11.002

Trachsel, M., Grosjean, M., Schnyder, D., Kamenik, C., and Rein, B., 2010, Scanning reflectance spectroscopy (380-730 nm): a novel method for quantitative high-resolution climate reconstructions from minerogenic lake sediments: Journal of Paleolimnology, v. 44, no. 4, p. 979-994. doi: 10.1007/s10933-010-9468-7

UNSCEAR (United Nations Scientific Committee on the Effects of Atomic Radiation), 2000, Sources and effects of ionizing radiation: United Nations. (accessed

USGS, 2010, Earthquake Hazards Program: M 8.8 - offshore Bio-Bio, Chile: https://earthquake.usgs.gov/earthquakes/eventpage/official20100227063411530_30#executive (accessed January 2018)

Van Daele, M., et al., 2016, Late Quaternary evolution of Lago Castor (Chile, 45.6°S): Timing of the deglaciation in northern Patagonia and evolution of the southern westerlies during the last 17 kyr: Quaternary Science Reviews, v. 133, p. 130-146. doi: 10.1016/j.quascirev.2015.12.021

Zolitschka, B., Francus, P., Ojala, A. E. K., and Schimmelmann, A., 2015, Varves in lake sediments – a review: Quaternary Science Reviews, v. 117, p. 1-41. doi: 10.1016/j.quascirev.2015.03.019